ISBN: 978-3-95450-234-9 ISSN: 2673-5504 doi:10.18429/JACoW-SRF2023-WEIXA03

OPTIMIZING THE MANUFACTURE OF HIGH-PURITY NIOBIUM SRF CAVITIES USING THE FORMING LIMIT DIAGRAM: A CASE STUDY OF THE HL-LHC CRAB CAVITIES RFD POLE*

Adrià Gallifa-Terricabras†,[1], Joanna Sylwia Święszek[1,2], Eduardo Cano-Pleite[3], Marco Garlaschè[1], Simon Barrière[1], Laurent Prever-Loiri[1], Stephan Pfeiffer[1], Ignacio Avilés Santillana[1], Manuele Narduzzi[4]
[1]European Organization for Nuclear Research (CERN), Geneva, Switzerland
[2]Kraftanlagen Nukleartechnik GmbH, Heidelberg, Germany
[3]Universidad Carlos III, Madrid, Spain
[4]Fermi National Accelerator Laboratory (Fermilab), Batavia, USA

Abstract

The Crab Cavities are key components of the High Luminosity Large Hadron Collider (HL-LHC) project at CERN, whose goal is to increase the integrated luminosity of the LHC, the world's largest particle accelerator, by a factor of ten. This paper explores the application of the Forming Limit Diagram (FLD) to enhance the manufacturing process of complex-shaped Nb-based crab cavities, with a focus on the formability challenges experienced with the pole of the RFD (Radio Frequency Dipole) Crab Cavities. The study includes the materials characterization of ultra-high-purity niobium (RRR300) sheets, namely mechanical tests and microstructural analysis; it also contains large-deformation Finite Element simulations of the pole deep drawing process, and the translation of the resulting strains in a FLD, together with several suggestions on how to improve the manufacturing process of such deep drawn parts. The results of this study can provide valuable insights for improving the design and fabrication of complex-shaped superconducting RF cavities made by large-deformation metal-sheet forming processes.

INTRODUCTION

The Crab Cavities are crucial devices to be installed in the High-Luminosity Large Hadron Collider (HL-LHC) at CERN, the upgraded version of the LHC. The goal of these complex-shaped cavities (see the RFD type in Fig. 1), which are made of 4 mm thickness sheets of ultra-high-purity niobium (RRR300), is to generate transverse electromagnetic fields that rotate the particle bunches longitudinally, such that they effectively collide head on, overlapping perfectly at the collision points (IR1 and IR5 of LHC) thus increasing the luminosity [1].

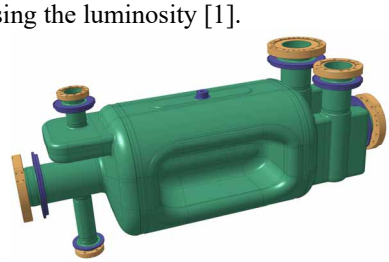

Figure 1: 3D View of bare RFD Crab Cavity. Courtesy R. Leuxe.

The cavities are operated at 1.9 K and are surrounded by a cold magnetic shield and a He tank, equipped with corresponding RF ancillaries, and hosted by a cryomodule containing the RF lines, cold and warm magnetic shield, thermal screen, cryogenic lines, tuning system, instrumentation for alignment and monitoring, among other devices [2].

Manufacturing Crab Cavities and RFD Pole

The manufacturing of Crab Cavities consists of a multi-technology process involving metal sheet forming (deep drawing, bending, extrusion), electron beam welding, vacuum brazing, machining, and surface processing such as Buffered Chemical Polishing (BCP).

The RFD Pole is one of the Crab Cavity sub-components experiencing the highest levels of deformation [3, 4], also along different strain paths, rendering it an object of study for pushing the understanding of Nb formability limits.

In the past, multiple studies have been conducted in order to understand the deep drawing of Niobium, including characterization of mechanical properties, FE simulations [3], friction studies [5], surface pollution studies, among others. Recent publications [6] introduce an experimental Forming Limit Curve (FLC) for 1 mm thickness RRR300 Nb sheets. However, the application of FE simulations incorporating the FLC for thicker Nb sheets (up to 4 mm thickness) for forming processes associated with SRF have not been studied before.

Challenges During Pole Forming

During the deep drawing of sub-components for RFD pre-series cavities at Zanon Research & Innovation (Zanon) -industrial partner of Fermilab within US HL-LHC AUP collaboration- some Poles manufactured using material from a specific batch (hereafter called Lot-2) exhibited orange peel appearance and experienced excessive thickness reduction in certain areas (minimum thickness around 2.3 mm), accompanied by the presence of wrinkles (as shown in Fig. 2).

*Work supported by CERN HL-LHC WP4
† adria.gallifa@cern.ch

ISBN: 978-3-95450-234-9 ISSN: 2673-5504 doi:10.18429/JACoW-SRF2023-WEIXA03

Figure 2: Detail of an RFD Pole showing excessive local thinning, orange peel and wrinkles. Courtesy Zanon and FNAL.

Consequently, the shape accuracy of these parts could not be guaranteed, and doubts about the material properties were raised. The issues were solved by applying a 2-step forming process, as described in the next paragraphs.

MATERIALS AND METHODS

Pole Forming Benchmark with Two Material Lots

Fermilab and CERN agreed to conduct an RFD Pole forming trial at CERN EN-MME Main Workshop. The objective of the trial was to compare the formability of two distinct material batches of 4 mm nominal thickness. A Nb RRR300 sheet from Lot-2 (previously showing difficulties during forming of pre-series cavities at Zanon) was used on one hand, together with a sheet from another lot (hereafter Lot-1) employed as reference. Both sheets were purchased, in the framework of HL-LHC Crab Cavities project, according to CERN material specification No. 3300 Ed. 4 [7] and were supplied by OTIC Ningxia. During forming of the RFD Pole, a bronze blank is used to maintain the Nb sheet in position during the process. A urethane film -placed between Nb sheet and the mold- as well as grease (industrial tallow) are used to avoid direct metal-to-metal contact in the RF surface and ensure a proper lubrication of all parts during the process, respectively [3] (see Fig. 3). The whole deformation process lasts typically between 60 and 120 seconds.

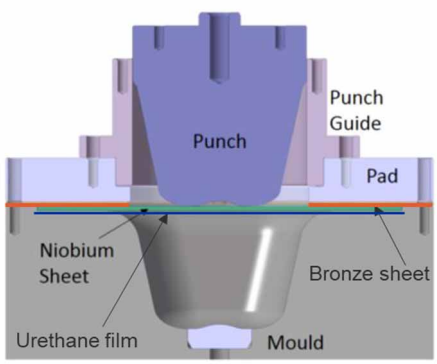

Figure 3: Schema of the initial configuration of the Pole forming and its constituent elements.

Forming trials were performed keeping the same process parameters: press machine, tools, molds, punch speed and operator; the only significant difference between the two tests being the material lot employed. Figure 4 shows good formability for the Pole made with Lot-1 material; in contrast, the Pole formed with Lot-2 showed a crack at the radius between the short lateral face and the horizontal face (presumably starting at one corner), and significant wrinkles in the base.

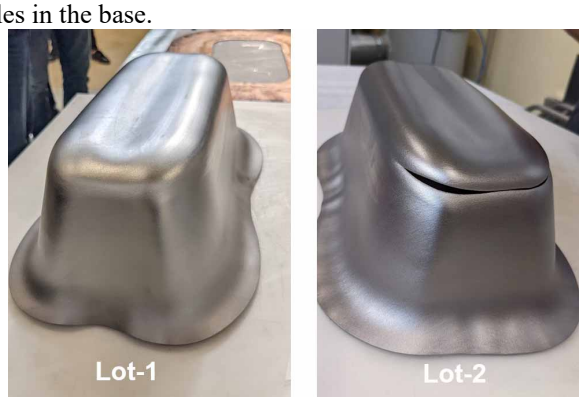

Figure 4: Deep drawing comparison with two material lots. Lot-2 shows a big crack on the upper part of the Pole (corner) as well as wrinkles in the base.

Use of the Forming Limit Diagram (FLD) for SRF Cavities

The Forming Limit Diagram (FLD) is a failure model applied to sheet-like materials; it is used to predict the feasibility of a forming process showing linear (monotonically increasing) strain paths [8].

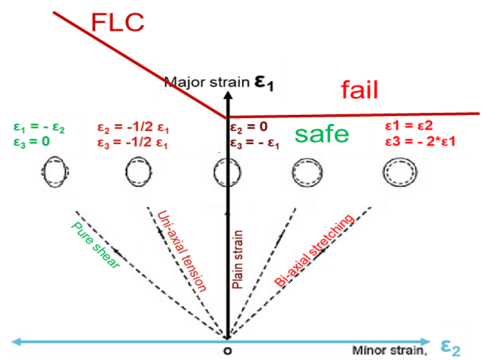

Figure 5: Schematic Forming Limit Curve (FLC) indicating different strain paths for an isotropic material.

A FLD is represented with ε_1 (major true strain) in the vertical axis) and ε_2 (minor true strain) in the horizontal axis; it typically contains the FLC (see Fig. 5) which establishes the onset of necking (start of inhomogeneous plastic deformation), and it can also contain the Forming Fracture Limit (FFL) which determines the ultimate failure strain threshold for a given material.

In this paper, a simplified approach, using Storen-Rice and Swift-Hill models, as presented in [8-11] are employed to estimate the FLC from a material property obtained by uni-axial tensile tests, namely the strain hardening coefficient *n* (considering a power law stress-strain curve). Such approach is used typically for isotropic materials and represents a preliminary way to estimate the forming limit curve and, in the present case, presumably explain the differences in formability between Lot-1 and Lot-2.

ISBN: 978-3-95450-234-9 ISSN: 2673-5504 doi:10.18429/JACoW-SRF2023-WEIXA03

The authors belief that the utilization of finite element (FE) simulations, coupled with a tailored failure criteria for membrane-like materials, such as the Forming Limit Diagram, can significantly contribute to comprehending and enhancing the formability of SRF cavities (either made of bulk niobium or copper).

Materials Testing

The metallographic preparation for Electron Backscatter Diffraction (EBSD) consisted in grinding with SiC paper up to P2400 and intermediate etching with a mixture of commercial acids HF:HCl:HNO_3 in the proportion 1:2:3, and final polishing step with colloidal silica (for about 10 min). For the EBSD analysis, performed with a field emission scanning electron microscope (FE-SEM Sigma by Zeiss) and an EBSD Nordlys detector by Oxford Instruments; 20 kV, a tilt angle of 70° and an aperture of 120 µm were used; 5 um step size was employed in order to obtain multiple data points per grain.

Tensile tests were performed with a universal testing machine Zwick&Roell-250 equipped with hydraulic grips and a video-extensometer. Specimen geometry was according to ASTM E8 subsize (i.e. b=6 mm, t=4 mm, L0=25 mm, Lc=32 mm); the strain rate employed was within the limits defined in ASTM B393 [12]: 0.007 min^{-1} ($1x10^{-4}$ s^{-1}) up to the yield strength and 0.05 min^{-1} ($8.3x10^{-4}$ s^{-1}) up to failure, with a smooth transition between both.

Finite Element Simulations

Finite Element Simulations of the RFD Pole deep drawing were performed using LS-Dyna software. This preliminary analysis assumed isotropic material properties for Nb sheet, using *MAT-PIECEWISE-LINEAR-PLASTICITY material model, which allows to input an experimental stress-strain curve and incorporates isotropic hardening by default. A representative curve for Lot-1 and Lot-2, respectively, were employed for obtaining the results displayed in the following sections. Different coefficients of friction (CoF) were employed for comparison (0.03 and 0.18) which are based on representative values found in previous tribological experiments [4]. A double symmetry was employed (thus results for one quarter of the Pole are presented). The surfaces in contact with Nb during forming (i.e. mold, punch and bronze blank) were also included in the simulations.

Fully integrated shell elements (ELFORM _16) were used, with mesh element size ~3 mm. For each element, the corresponding ε_1-ε_2 pair (in the mid-thickness) was plotted in the FLD, thus obtaining a cloud of points for the quarter of the Pole at the end of the process. It is to be noted that with the above-mentioned conditions, the ε_1-ε_2 pairs were increasing linearly and monotonically for different representative regions of the Pole, therefore the use of FLD is considered appropriate for the present case.

RESULTS AND DISCUSSION

Initial Sheets Material Properties

The material supplier claimed that both Lot-1 and Lot-2 had followed multiple cross-directional rolling steps (however, the exact traceability of the rolling steps, its orientation and thickness reduction per rolling pass is unknown). Therefore, in this work, the rolling direction (RD) has been adopted by convention as the longest direction of the sheets. The supplier also claimed that the total area reduction for both sheets was similar, as well as the annealing heat treatments. Also, a final single-direction levelling step was reported. Some initial sheet parameters are displayed in Table 1.

Table 1: Initial parameters. Ra values measured at least in 3 random locations (in both RD and TD, and both sheet surfaces). Sheet thickness from specimens cut at random positions. RRR values from the material certificate type 3.1 (EN 10204).

	Initial Sheet size [mm]	Initial surface roughness (Ra) [µm]	Initial sheet thickness [mm]	RRR [-]
Lot-1	700x1000x4	0.75 ± 0.15	3.96 ± 0.01	308 - 433
Lot-2	600x1200x4	0.63 ± 0.13	3.97 ± 0.03	332

Microstructure, Texture, and Hardness Profiles

Inverse Pole Figure (IPF) maps from Y direction (Normal Direction, ND), are presented in Fig. 6 for a representative sample of both lots studied; the surface presented is in the X (RD) -Y (ND) plane.

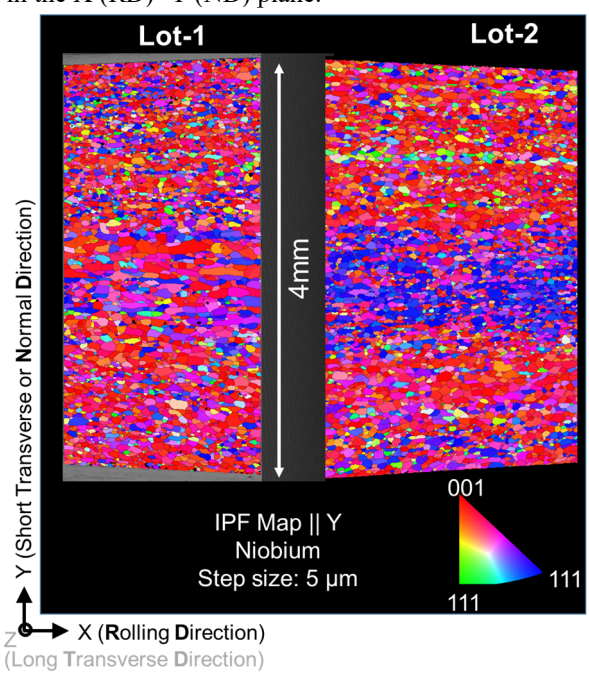

Figure 6: Full thickness IPF Maps || ND (or Y) for Lot-1 (left) and Lot-2 (right) 4 mm sheets in as-received (annealed) condition.

ISBN: 978-3-95450-234-9 ISSN: 2673-5504 doi:10.18429/JACoW-SRF2023-WEIXA03

Additionally, the corresponding IPF plots in three orthogonal directions are shown in Fig. 7.

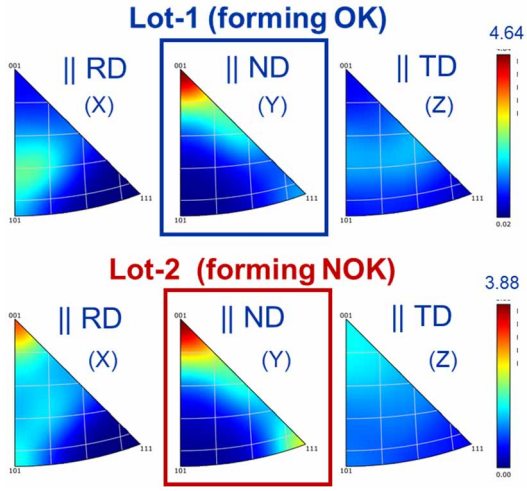

Figure 7. Inverse Pole Figures (IPF) along X (RD), Y (ND) and Z (TD) for samples displayed in Fig. 6. Color-scale indicates texture intensity.

In the IPF plots, Lot-1 shows a rather random crystal orientation || RD and || TD, and a stronger (001) texture || ND. Lot-2 shows a significant texture intensity of type (001) in all directions, as well as a clear banded texture through thickness (|| ND): (001) band on the top surface + (111) band at mid-thickness + (001) band on the bottom surface. In the literature, texture inhomogeneity through the thickness of Nb sheets of 2 mm thickness was also reported, although (111) texture was predominant [13, 14].

The grain size, obtained after EBSD measurements, is summarized in Table 2.

Table 2: Grain size results (threshold angle = 10°) obtained by EBSD for cross sections parallel to the RD-ND plane (0°) and TD-ND plane (90°).

Equivalent grain size	Mean [µm]	Std. Dev. [µm]	Max. [µm]
Lot-1_0°	41	22	232
Lot-1_90°	39	18	174
Lot-2_0°	45	23	222
Lot-2_90°	44	21	286

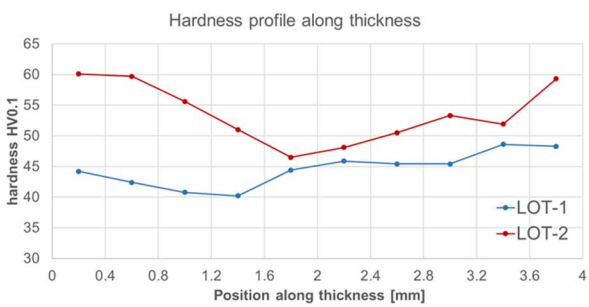

Figure 8: Hardness (HV0.1 kg) profiles along sheet thickness. Done according to ISO 6507-1.

Lot-1 has, in average, a slightly reduced grain size (in the EBSD Map shows smaller and equi-axed grain size towards the surface and larger and elongated in the mid-thickness) with respect to Lot-2 (which has larger size grains towards the surface with respect to Lot-1). The overall largest grains are also found in Lot-2. A hardness profile along the sheet thickness is presented in Fig. 8. For Lot-2, a "V-shape" is present, suggesting that the levelling step was more pronounced, in comparison to Lot-1.

The microstructural differences (grain size distribution along thickness), together with inhomogeneous texture (different texture bands through thickness), are presumably linked to varying anisotropy values for both sheets and thus, might produce different macroscopic behavior during forming. This topic has been extensively investigated by [13, 15] and is subject of interest for future research on the present material lots.

Tensile Tests

Tensile tests results for Lot-1 and Lot-2 at 0 and 90° are shown in Table 3 and Table 4, respectively, and the corresponding true stress-strain curves are displayed in Fig. 9. Some significant differences between the two lots are the strain hardening coefficient *n (0.35-0.38* for Lot-1 vs. *0.28-0.30* for Lot-2) as well as the Rp0.2/Rm ratio (0.31-0.33 for Lot-1 vs. 0.42-0.50 for Lot-2); these results being in line with [14].

Elongation at Break is, counterintuitively, higher for Lot-2, although this parameter presents typically a significant variability due to the specific size and location of the necking with respect to the specimens' gauge length.

Table 3: Tensile test results for Lot-1; 2x specimens cut along the RD (0°) and 2x in the TD (90°).

Specimen	$R_{p0.2}$ [MPa]	R_m [MPa]	A_g [%]	A_{25mm} [%]	$n_{0.02-0.20}$ [-]	$R_{p0.2}/R_m$ [-]
Lot1_0°-1	53.0	161.6	30.9	52.6	0.38	0.33
Lot1_0°-2	49.5	159.4	33.0	62.3	0.38	0.31
Lot1_90°-1	51.4	167.7	31.3	59.2	0.37	0.31
Lot1_90°-2	53.6	166.6	27.9	55.1	0.35	0.32

Table 4: Tensile test results for Lot-2; 2x specimens cut along the RD (0°) and 2x in the TD (90°).

Specimen	$R_{p0.2}$ [MPa]	R_m [MPa]	A_g [%]	A_{25mm} [%]	$n_{0.02-0.20}$ [-]	$R_{p0.2}/R_m$ [-]
Lot2_0°-1	68.7	164.5	32.4	64.9	0.30	0.42
Lot2_0°-2	69.1	160.0	32.3	69.7	0.29	0.43
Lot2_90°-1	74.0	163.0	29.5	61.6	0.28	0.45
Lot2_90°-2	80.9	162.8	29.9	59.9	0.28	0.50

It must be noted that the Rp0.2 of Lot-1 falls below the specified limit of 65 MPa mentioned in the CERN material specification [7] but Lot-2, which showed poor formability, is compliant with the above-mentioned specification.

ISBN: 978-3-95450-234-9 ISSN: 2673-5504 doi:10.18429/JACoW-SRF2023-WEIXA03

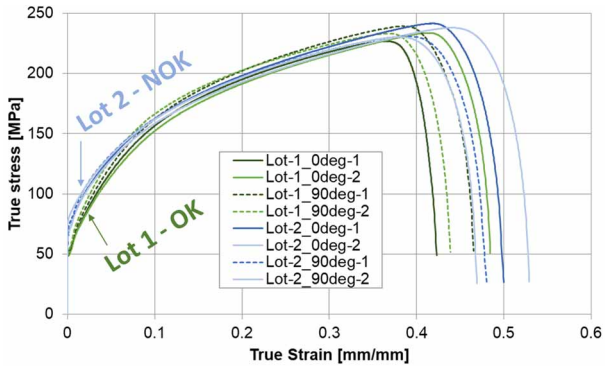

Figure 9: Comparison of true stress-strain curves for Lot-1 (green) and Lot-2 (blue) specimens. Both lots exhibit a similar trend, with Lot-1 displaying a lower Rp0.2.

FE Simulations Considering Isotropic Material Properties

The results of the FE simulations showing ε_1-ε_2 pairs for each element of the Pole (cloud of blue points), together with the estimation of the FLC are presented in Fig. 10.

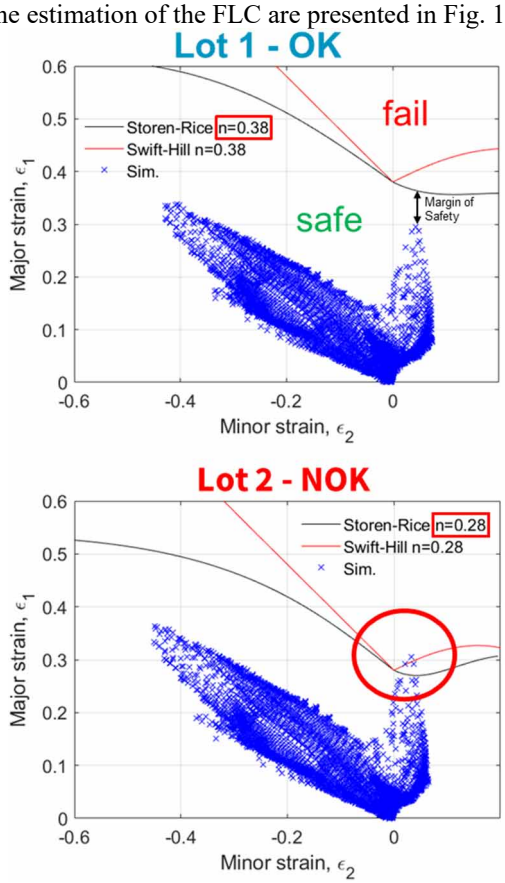

Figure 10: Comparison of Pole forming (pairs of ε_1-ε_2 for each element) placed in a FLD for Lot-1 (Top) with Lot-2 (Bottom), considering a CoF=0.18. Theoretical FLC curves were build using strain hardening index, *n,* with Storen-Rice and Swift-Hill models, respectively.

In both cases the clouds of points present the same trend: most elements fall in strain paths between pure shear and compression (safe zone of the FLD), however, there is a critical zone that is submitted to plane-strain and biaxial strain paths ($\varepsilon1 \sim 0.3$; $\varepsilon2 \sim 0$ to - 0.05). This critical zone coincides with the corners of the Pole where the cracks appeared, see Fig. 4. Due to the difference in strain hardening coefficient, n, the cloud of points for Lot-1 is not reaching the FLCs, whereas for Lot-2 few points are crossing the FLCs, indicating a potential failure.

CONSIDERATIONS FOR OMPTIMIZING THE FORMING OF SRF CAVITIES

Effect of Friction in the FLD

The influence of the coefficient of friction (CoF) on the process feasibility was simulated (Figure 11).

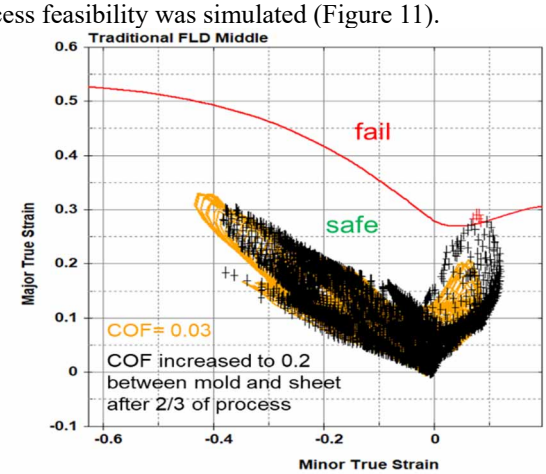

Figure 11: Pole forming with Lot-2 material; effect of increasing the Coefficient of Friction (CoF) represented in the FLD.

CoF between Nb sheet and the mold was increased from 0.03 to 0.2 at two-thirds (2/3) of the process (replicating an eventual breakage of the urethane film or a sudden reduction of the lubrication). As expected, this parameter is found to have a high impact on the formability. The maximum ε_1 at the critical zones -plane-strain and biaxial- is significantly increased (by a 50%).

2-Step Forming: Effect of Trimming Before Reaching Final Shape

Zanon adopted a 2-step forming process (see Fig. 12) consisting of: forming and stopping before reaching the final shape (at ~10 mm before the punch reaches the maximum displacement), trimming the upper leftovers, re-greasing all the parts and complete the forming until the final shape.

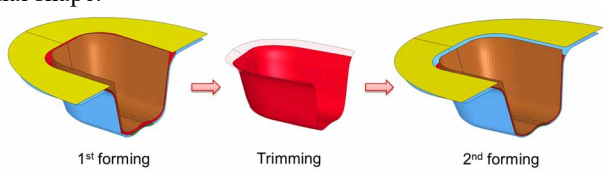

Figure 12: Schema of the 2-step forming process.

Therefore, the strategy proposed has a double potential benefit: not only re-lubricating the parts (beneficial as shown in the previous section), but also performing trimming to improve the material flowability.

ISBN: 978-3-95450-234-9 ISSN: 2673-5504 doi:10.18429/JACoW-SRF2023-WEIXA03

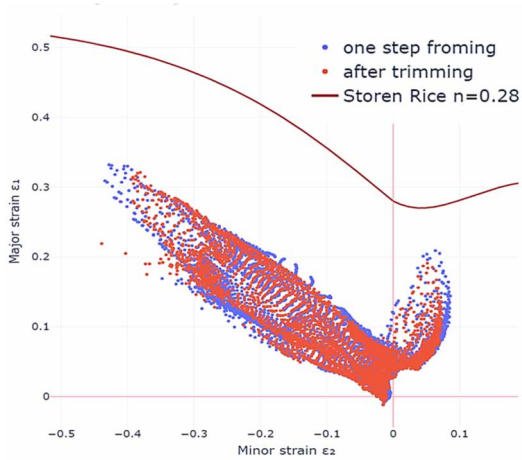

Figure 13: 2-step forming slightly reduces the value of strain in the conflictive region. CoF was kept constant.

The simulations, although preliminary, indicate a slight improvement thanks to the trimming itself (see Fig. 13). It is believed that a more complete material model (including anisotropy and strain rate sensitivity effects) might help better understanding this process and is subject of ongoing and future research by the authors.

CONCLUSIONS AND FUTURE WORK

In this work, an exhaustive comparison of two material lots –that present significant different formability behavior- was performed, including microstructure and texture analysis along with mechanical properties (hardness profiles, tensile tests). Additionally, Finite Element Simulation results compared against estimated theoretical FLC curves were presented.

After assessing the discrepancies in material properties and the preliminary FE simulation results, the differences in formability between Lot-1 (good formability) and Lot-2 (poor formability) can arise from the combination of the following aspects:

- Difference in mechanical properties (stress-strain curves), namely the strain hardening index, *n*, and the Rp0.2/Rm ratio.
- Hardness profiles show that Lot-2 has presumably seen a more pronounced levelling step.
- In terms of microstructure, the mean grain size is slightly smaller for Lot-1, especially towards the surface. On the other hand, it has a more random crystal orientation viewed from RD and TD, a (001) peak intensity is only observed from ND. Lot-2 presents a texture of grains oriented preferentially in (001) from all directions, as well as a banded structure parallel to the surface, when observed along ND, and slightly larger grains towards the surface.
- From the FE simulations it is noted that the coefficient of friction has a strong effect in shifting vertically (i.e. increase ε1) the cloud of points corresponding to elements submitted to plane-strain and biaxial condition. Different phenomena could play a role in varying the CoF during the forming process: local thickness variations among a sheet (local thicker sheet thickness and resulting reduced gap with the mold will lead to increased friction), the type and quantity of grease used, the initial surface roughness, etc.

About the strategy used to improve formability:

- The effect of 2-step forming, employed to improve the formability of real parts, has presumably a double beneficial effect: reduce the CoF of the top leftovers in contact with the bronze sheet (improving material flowability), and reduce CoF due to the re-greasing of all parts before completing the forming process.

The use of FE simulations together with the FLD has proven to show useful complementary information with respect to 'conventional' FE simulation results (which usually display the effective plastic strain and thickness variation).

Nb is known to be a relatively high strain rate sensitive material, and typically shows significant anisotropic behavior (relationship between microstructure and anisotropy for pure Nb has been extensively investigated by [15]). To achieve a more precise and comprehensive material model that incorporates these characteristics in the finite element (FE) simulations, the authors are currently conducting tensile tests with Digital Image Correlation (DIC) at higher strain rates. These tests include measurements at 0, 45, and 90° angles relative to the rolling direction to determine the corresponding anisotropy r-values (Lankford coefficients). Additionally, experimental determination of the FLC for both lots is envisaged to complete and fully validate this study.

ACKNOWLEDGEMENTS

To Stefano Sgobba, Nuria Valverde for the useful discussions and technical advice; Bartosz Bulat for the roughness measurements, Leonardo Ristori, Paolo Berrutti (Fermilab) for triggering the matter and allowing CERN to investigate these Pole forming issues; Paolo Barbero, Marco Raumer, Mauro Festa from Zanon to report challenges about the initial forming and to share the process employed to improve it; OTIC Ningxia and Elite Materials Solutions Ltd. for facilitating additional information regarding the material lots used; Rama Calaga, Ofelia Capatina, Said Atieh, for funding and supporting this research within HL-LHC WP4 and EN-MME group.

REFERENCES

[1] O. Brüning and L. Rossi, "High-Luminosity Large Hadron Collider", CERN Yellow Reports: Monographs, vol. 10, pp. 1-1, 2020. doi:10.23731/CYRM-2020-0010.1

[2] T. Capelli *et al.*, "Design of Crab Cavity Cryomodule for HL-LHC", in *Proc. SRF'19*, Dresden, Germany, Jun.-Jul. 2019, pp. 320-325. doi:10.18429/JACoW-SRF2019-MOP099

[3] A. Amorim Carvalho *et al.*, "Advanced design of tooling for sheet-metal forming through numerical simulations in the scope of SRF crab cavities at CERN", in *AIP Conf. Proc.*, vol. 2113, no. 1, p. 100008, 2019. doi:10.1063/1.5112641

ISBN: 978-3-95450-234-9 ISSN: 2673-5504 doi:10.18429/JACoW-SRF2023-WEIXA03

[4] A. Gallifa Terricabras *et al*., "Assessment of the Mechanical Properties of Ultra-High Purity Niobium After Cold Work and Heat Treatment With the HL-LHC Crab Cavities as Benchmark", in *Proc. SRF'19*, Dresden, Germany, Jun.-Jul. 2019, pp. 860-865. doi:10.18429/JACoW-SRF2019-THP012

[5] A.T. Silvestri *et al*., "Understanding the Friction Behavior of Niobium Sheets during Forming Processes", *J. Mater. Eng. Perform.*, vol. 29, pp. 3055-3066, 2020. doi:10.1007/s11665-020-04868-w

[6] J.F. Croteau *et al*., "Characterization of the Formability of High-Purity Polycrystalline Niobium Sheets for Superconducting Radiofrequency Applications", *J. Eng. Mater. Technol.*, vol. 144, p. 021004, 2022. doi:10.1115/1.4052557

[7] CERN Material Specification, N° 3300 - Ed. 4, "Pure niobium sheets for superconducting applications", RRR 300 grade, EDMS 1095252, Geneva, Switzerland. https://edms.cern.ch/document/1095252

[8] S. K. Paul, "Theoretical analysis of strain-and stress-based forming limit diagrams", *J. Strain Anal. Eng. Des*., vol. 48, no. 3, pp. 177-188, 2013. doi:10.1177/0309324712468524

[9] S. Stören and J. R. Rice, "Localized necking in thin sheets", *J. Mech. Phys. Solids*, vol. 23, no. 6, pp. 421-441, 1975. doi:10.1016/0022-5096(75)90004-6

[10] R. Zhang, Z. Shao, and J. Lin, "A review on modelling techniques for formability prediction of sheet metal forming", *Int. J. Lightweight Mater. Manuf.*, vol. 1, no. 3, pp. 115-125, 2018. doi:10.1016/j.ijlmm.2018.06.003

[11] A. Gallifa-Terricabras *et al*., "Forming Limit Diagram of Annealed Cu-OFE Thick Sheets: A Novel Approach for Superconducting RF Cavities", submitted for publication.

[12] ASTM International, "ASTM B393-18 - Standard Specification for Niobium and Niobium Alloy Strip, Sheet, and Plate". doi:10.1520/B0393-18

[13] H. Jiang *et al*., "Mechanical properties of high RRR niobium with different texture", *IEEE Trans. Appl. Supercond*., vol. 17, no. 2, pp. 1291-1294, 2007. doi:10.1109/TASC.2007.898463

[14] C. Antoine, "Materials and surface aspects in the development of SRF Niobium cavities", *EuCARD editorial series on accelerator science*, 12 No. EuCARD-BOO-2012-001, 2012. http://cds.cern.ch/record/1472363

[15] A. Zamiri and F. Pourboghrat, "Characterization and development of an evolutionary yield function for the superconducting niobium sheet", *Int. J. Solids Struct*., vol. 44, no. 25-26, pp. 8627-8647, 2007. doi:10.1016/j.ijsolstr.2007.06.025